

Dynamic palmitoylation events following T-cell receptor signaling

Eliot Morrison¹, Tatjana Wegner¹, Andres Ernesto Zucchetti², Miguel Álvaro-Benito ¹, Ashley Zheng¹, Stefanie Kliche³, Eberhard Krause⁴, Britta Brügger⁵, Claire Hivroz² & Christian Freund¹✉

Palmitoylation is the reversible addition of palmitate to cysteine via a thioester linkage. The reversible nature of this modification makes it a prime candidate as a mechanism for regulating signal transduction in T-cell receptor signaling. Following stimulation of the T-cell receptor we find a number of proteins are newly palmitoylated, including those involved in vesicle-mediated transport and Ras signal transduction. Among these stimulation-dependent palmitoylation targets are the v-SNARE VAMP7, important for docking of vesicular LAT during TCR signaling, and the largely undescribed palmitoyl acyltransferase DHHC18 that is expressed in two isoforms in T cells. Using our newly developed On-Plate Palmitoylation Assay (OPPA), we show DHHC18 is capable of palmitoylating VAMP7 at Cys183. Cellular imaging shows that the palmitoylation-deficient protein fails to be retained at the Golgi and to localize to the immune synapse upon T cell activation.

¹Freie Universität Berlin, Institute for Chemistry & Biochemistry, Laboratory of Protein Biochemistry, Thielallee 63, 14195 Berlin, Germany. ²Institut Curie, PSL Research University, INSERM U932, Integrative analysis of T cell activation team, 26 rue d'Ulm, 75248 Paris Cedex 05, France. ³Otto-von-Guericke-University, Institute of Molecular and Clinical Immunology, Health Campus Immunology, Infectiology and Inflammation, Leipziger Strasse 44, 39120 Magdeburg, Germany. ⁴Leibniz Institute for Molecular Pharmacology, Mass Spectrometry Unit, Robert-Rössle-Str 10, 13125 Berlin, Germany. ⁵Heidelberg University Biochemistry Center (BZH), Im Neuenheimer Feld 328, 69120 Heidelberg, Germany. ✉email: chfreund@zedat.fu-berlin.de

The initial signaling events following the recognition of a peptide-MHC complex on an antigen-presenting cell (APC) by the T-cell receptor (TCR) involve a number of important molecules that must localize to the plasma membrane (PM) at the immunological synapse (IS). Palmitoylation, the reversible linking of 16-carbon palmitic acid to cysteines via a labile thioester bond, is one strategy used by several important TCR-signaling proteins to drive this localization to and from the membrane (e.g., the soluble Src-family kinases Lck and Fyn) or to and from liquid-ordered microdomains (“lipid rafts”) within the membrane (e.g., the transmembrane scaffold LAT)¹.

Unlike other lipid modifications like myristoylation or prenylation, the reversible chemistry of the thioester bond allows palmitoylation to be both added to and removed from specific cysteines; indeed, enzymes have evolved to both add (e.g., the DHHC family of protein acyltransferases [PATs]) and remove (e.g., acyl protein thioesterase 1 [APT1] and ABHD17) palmitate from these sites in eukaryotes^{2,3}. This has given rise to palmitoylation cycles, where proteins are palmitoylated in the ER/Golgi, cycled to the PM via vesicle trafficking and localized to the site of activity, then depalmitoylated and recycled back to the ER/Golgi⁴.

Such cycles have become well established in neuronal proteins like PSD-95, as well as the G-protein α subunits $G\alpha_i$ and $G\alpha_q$ and small GTPases H-Ras and N-Ras^{4,5}, and pulse-chase experiments have shown that palmitoylation turnover can be accelerated following signaling stimuli, such as glutamate receptor activation with PSD-95, GTP binding of H-Ras, and GPCR signaling for $G\alpha$ proteins^{6–8}. In the context of T-cells, Lck has been shown to undergo relatively rapid palmitate turnover under resting conditions, which is accelerated following Fas receptor stimulation, and this palmitoylation is specifically catalyzed by DHHC21 at the PM⁹. A decrease in the palmitoylation of LAT has been observed in anergic T cells, which affects its ability to localize to lipid rafts and induce an effective stimulatory response^{1,10}. Docking of vesicular LAT to the IS and downstream signaling also critically depend on palmitoylated SNARE proteins like SNAP-23 and VAMP7^{11,12}. While these targeted approaches suggest the possibility of regulated palmitoylation cycles, a global approach tracking changes of the complete palmitome of T cells following a stimulatory event has not been reported.

Equally enigmatic are the enzymes responsible for catalyzing the palmitoylation reaction, the DHHC family of PATs, first identified in yeast more than 15 years ago^{13,14}. While 23 PATs are expressed in mammals, due to the challenges inherent in expressing and purifying these multi-pass membrane proteins, only a handful of mammalian PATs have been investigated in vitro: the palmitoylation of $G\alpha_i$ by DHHC2 and DHHC3, the palmitoylation of PSD-95 by DHHC15, and the autopalmitylation of DHHC9 and DHHC20^{15–19}. These studies often rely on the use of [³H]-palmitic acid to quantify the palmitoylated substrate, requiring long exposure times and the hazards of radioactive materials, or else are limited to the kinetics of the autopalmitylation reaction using enzyme-linked assays or palmitoylation targets of peptide length. We here developed the on-plate palmitoylation assay (OPPA) method as a rapid, click chemistry-based approach to quantifying an intact palmitoylated substrate over time.

The understanding of palmitoylated SNARE proteins has generally been restricted to those lacking transmembrane domains (TMDs), such as SNAP-25 and the vesicular SNARE Ykt6, where the addition of hydrophobic palmitate assists in membrane recruitment²⁰. However, the vesicular synaptobrevin-family SNARE protein VAMP7, despite featuring a single TMD at its C-terminus, has been reported to be palmitoylated in a large number of different mammalian global palmitome studies^{21–30}.

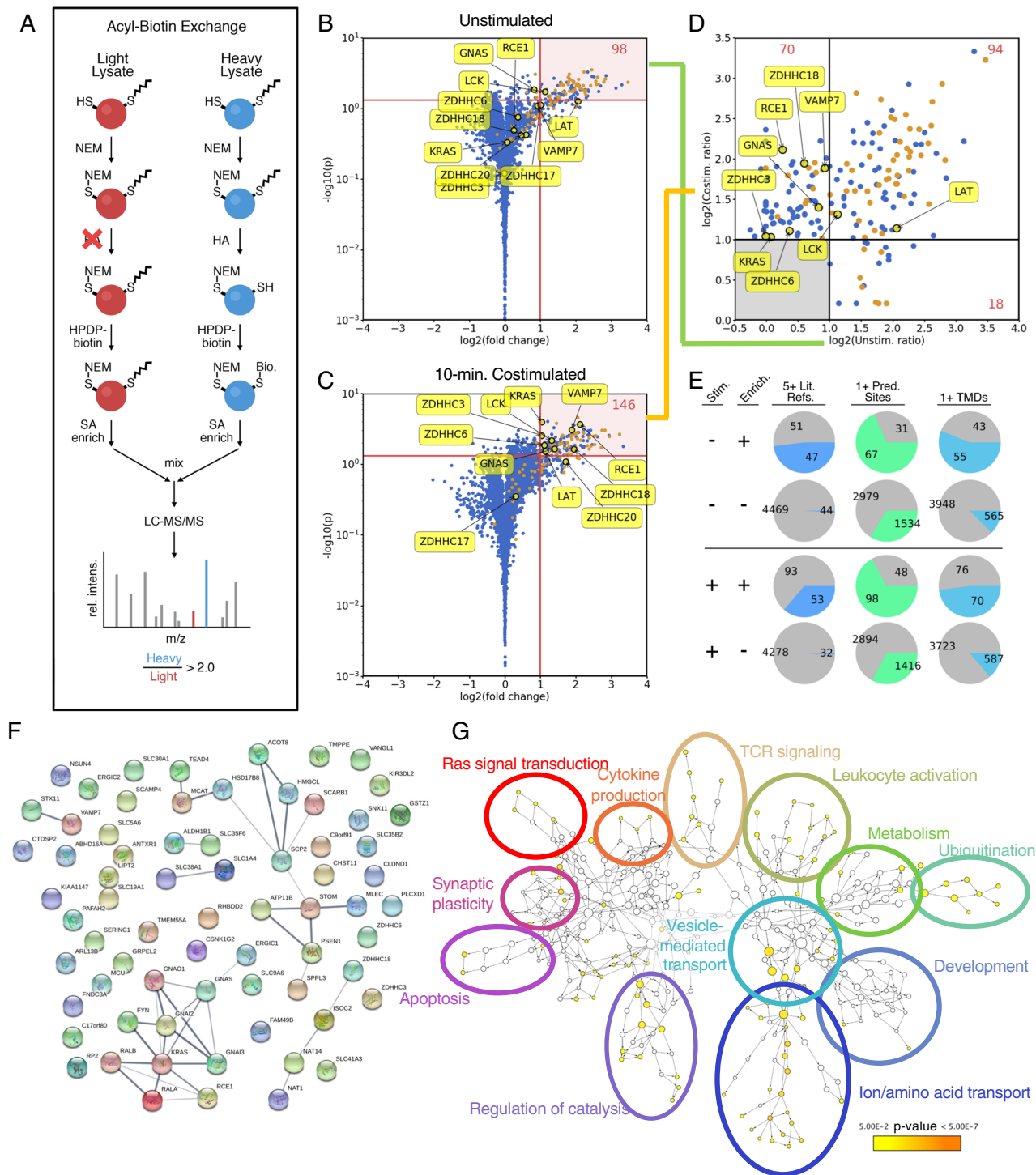
The observation that many of the proteins found to be palmitoylated are in fact integral membrane proteins (up to ~50–60% of proteins enriched by ABE) suggests the mechanism of regulated palmitoylation is subtler than the simpler model of membrane recruitment³¹. Possible reasons why a transmembrane protein might be palmitoylated include the mediation of protein-protein interactions within the membrane, the induction of conformational changes (e.g., “tilting” within the membrane or the recruitment of soluble tails to the membrane), the driving of localization to liquid-ordered microdomains within the membrane, or as an interplay with other post-translation modifications like ubiquitin³². The palmitoylation of VAMP7 might represent a new mode of transmembrane SNARE protein palmitoylation beyond the relatively straightforward membrane recruitment seen in the soluble SNARE proteins, allowing an additional layer of subtlety to its regulation.

Results and discussion

The T-cell palmitome composition changes on TCR stimulation. Using the acyl-biotin exchange (ABE) method with SILAC-labeled Jurkat T-cell lysates allowed us to quantify the T-cell palmitome via quantitative LC-MS/MS (Fig. 1a)³¹. We previously reported the ABE-enriched Jurkat palmitome under resting conditions³¹; here we reanalyze these data with a volcano plot-based approach, allowing us to identify 115 high-confidence palmitoylation candidates, including well-established palmitoylated proteins like Lck and LAT (Fig. 1b). This allows for the direct comparison to the Jurkat palmitome 10 min following anti-CD3/anti-CD28 costimulation (Fig. 1c and d, Supplementary Fig. 1). After stimulation, 169 proteins are found in the high-confidence palmitoylated pool. Three criteria were used for validation (Fig. 1e): number of previous reports in 13 human palmitome studies, number of predicted palmitoylation sites (CSSPalm 4.0), and number of predicted transmembrane domains (TMDs) (TMHMM 2.0); we see an over-representation of all three criteria in our enriched pools versus background unenriched proteins, confirming the enrichment^{27,28,30,31,33–43}.

Directly comparing these two pools of proteins reveals 94 constitutively palmitoylated proteins, 18 stimulation-dependent depalmitoylated proteins, and 70 stimulation-dependent modified proteins (Supplementary Data 1). Lck and LAT are constitutively palmitoylated, while among the stimulation-dependent palmitoylated proteins are the v-SNARE protein VAMP7 and the PAT DHHC18. VAMP7 belongs to the synaptobrevin family of v-SNAREs, and has been shown to be crucial for docking vesicular LAT to the IS and downstream signaling events in CD4+ T cells¹¹. DHHC18 is a Golgi-localized PAT, and although it has been described to palmitoylate H-Ras^{44,45}, little is known about its enzymatic properties or substrate specificity¹⁹. As autopalmitylation is the initial step in the PAT enzymatic mechanism⁴⁶, finding this PAT palmitoylated after TCR stimulation presumably represents an activated state of this enzyme, and may hint at an upregulation of specific PAT activity following TCR stimulation.

Of the stimulation-dependent palmitoylation candidates, approximately half are transmembrane proteins. Grouping the protein interaction networks using STRING analysis reveals a large cluster of $G\alpha$, Ras, and Ras-related proteins (Fig. 2a). Intriguingly, within this cluster are GNAI3, GNAO1, and GNAI1/2, all of which feature N-terminal myristoylation motifs, while the $G\alpha$ proteins GNAQ and GNA13, both of which lack a myristoylation motif, are found to be constitutively palmitoylated. This could suggest an interplay between co-translational myristoylation and post-translational, stimulation-dependent palmitoylation, in which myristoylated $G\alpha$ proteins are



preferentially palmitoylated following TCR stimulation. Indeed, the stimulation-dependent palmitoylation targets feature a slight enrichment of proteins containing myristoylation motifs (8.8%) versus constitutively palmitoylated proteins (6.4%), perhaps hinting at a larger trend. Functionally, the stimulation-dependent palmitoylation candidates are involved in a variety of cellular processes (Fig. 1g), notably Ras signal transduction, TCR-signaling, and vesicle-mediated transport.

Rapid determination of palmitoylation rates by OPPA. To investigate these stimulation-dependent palmitoylation candidates in a controlled setting, we designed constructs of DHHC18,

DHHC20, VAMP7, and LAT for expression in Sf9 insect cells (Fig. 2A, Supplementary Figs. 4, 5). Although VAMP7 has been reported as palmitoylated in eight other human palmitome studies^{23,24,27,28,30,38,39,43,47}, the site of its palmitoylation has not been described. Of the six cysteines in its primary sequence, we found three NEM-modified during our ABE enrichment (data not shown), suggesting they are not palmitoylated, while two others are located in the vesicular lumen, not accessible to a DHHC PAT's cytosolic active site; the remaining cysteine, Cys183, which is located in an optimal juxtamembrane position, was therefore chosen for mutational studies as the most likely site of palmitoylation³³.

Fig. 1 Enrichment of Jurkat T-cell palmitome before and after anti-CD28/anti-CD3-costimulation by acyl-biotin exchange. **a** Schematic representation of acyl-biotin exchange (ABE) protocol coupled with SILAC for quantitation of palmitoylated proteins via LC-MS/MS. Briefly, Jurkat cells grown in heavy SILAC media (blue) were lysed and free thiols were blocked with NEM. After cleaving palmitoyl groups with HA, previously palmitoylated thiols are biotinylated with HPDP-biotin, allowing for streptavidin enrichment. For control cells grown in light SILAC media (red), HA is omitted, preventing biotinylation. Proteins quantified with heavy/light intensity ratios >2.0 are considered enriched and palmitoylated. **b** Volcano plot showing high-confidence palmitoylated proteins prior to stimulation ($n = 6$, $p < 0.05$). Proteins found in five or more other palmitome studies are highlighted in orange. **c** Volcano plot showing high-confidence palmitoylated proteins 10 min after anti-CD28/anti-CD3 costimulation ($n = 4$, $p < 0.05$). **d** Comparison of high-confidence palmitoylated pools before and after stimulation. Only proteins from **b** and **c** that displayed a p -value < 0.05 are considered. These p -values and additional statistical parameters are detailed in Supplementary Data 1. **e** Analysis of palmitoylated proteins compared to unenriched (background) proteins, with three metrics: at least five references in previous palmitome studies, at least one predicted palmitoylation site (CSSPalm 4.0, high cutoff), and at least one predicted transmembrane domain (TMHMM 2.0). **f** STRING functional analysis of proteins enriched for palmitoylation 10 min after TCR stimulation. A clear cluster of $G\alpha$ and Ras-related proteins is observed. Several interesting candidates are highlighted, including VAMP7 and DHHC18, which were investigated in more detail in this study. **g** Gene Ontology (GO) term enrichment of stimulation-dependent palmitoylation candidates, generated using BiNGO. Cluster size indicates the number of genes in each node, while color indicates statistical significance of enrichment.

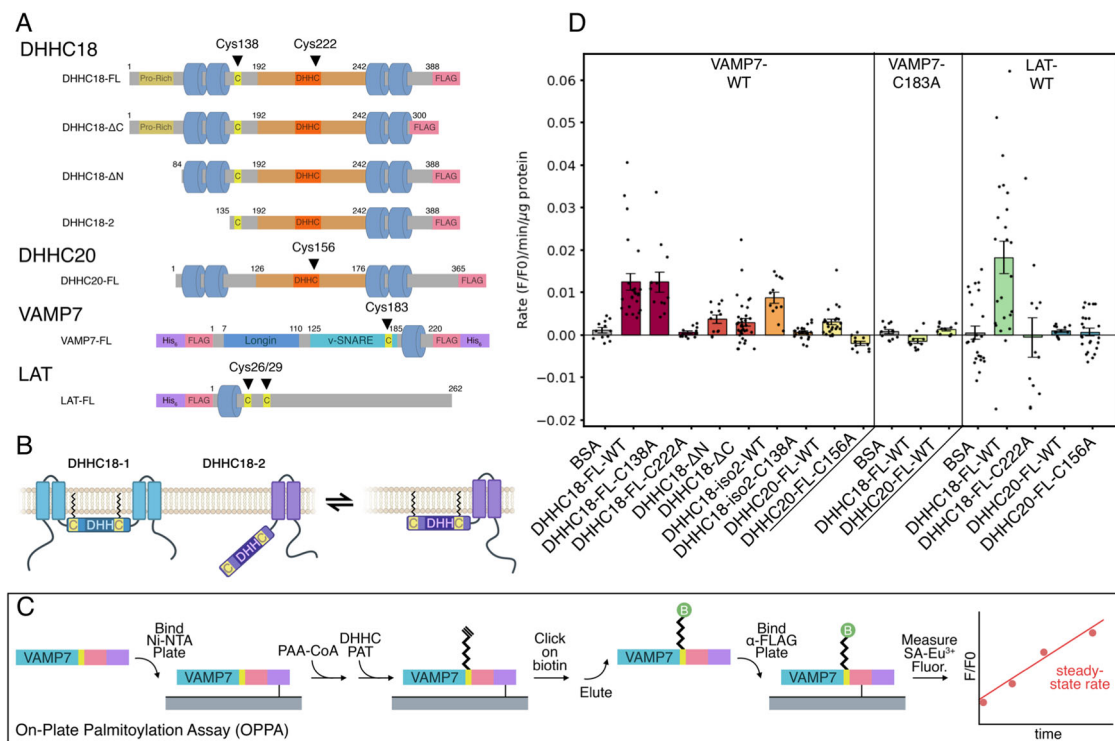


Fig. 2 In vitro palmitoylation of VAMP7 by DHHC18 and DHHC20. **a** Schematic cartoon of constructs used, with important cysteines highlighted. Cys222 and Cys15 are the active sites of DHHC18 and DHHC20, respectively. Cys183 in VAMP7 is the site of palmitoylation. **b** Cartoon model of potential membrane docking of DHHC18 isoform 2 via Cys138. The full-length DHHC18 features the two N-terminal TMDs, securing the DHHC active site to the membrane. The short isoform, lacking these TMDs, may be anchored to the membrane via palmitoylation of Cys138, allowing its active-site access to the membrane environment required for its activity. **c** Schematic representation of the on-plate palmitoylation assay (OPPA). Briefly, the target (VAMP7, featuring both His₆ and FLAG-tags) is bound to a Ni-NTA plate. The DHHC PAT is added with clickable PAA-CoA and the reaction is quenched at specific time points using NEM. Biotin is subsequently clicked on to the PAA-modified target, VAMP7 is eluted and then bound to an anti-FLAG plate. Streptavidin-Eu³⁺ can then be used to quantify palmitoylated VAMP7, and a steady-state slope can be calculated. **d** Results of OPPA experiments of VAMP7-WT and VAMP7-C183A, palmitoylated by constructs of DHHC18 and DHHC20 ($n \geq 12$, geometric mean \pm SEM shown).

Likewise, in DHHC18, we sought to investigate the role the N- and C-terminal tails of DHHC18 might play in the enzyme's stability or activity by designing ΔN and ΔC domain constructs. Moreover, we designed a construct based on the truncated isoform 2 of DHHC18, which we previously hypothesized was preferentially palmitoylated in T cells³¹. Intriguingly, this isoform lacks the two N-terminal TMDs of the full-length protein, yet features a cysteine (Cys138) only three residues from its new N-terminus, which might represent a palmitoylation anchor to the membrane.

In order to improve upon the shortcomings of current in vitro palmitoylation assays, we developed the OPPA method

(Fig. 2B). Briefly, purified substrates (e.g., VAMP7) bearing both His₆- and FLAG-tags are bound to Ni-NTA plates, to which purified DHHC PATs (lacking His₆-tags) and clickable palmitic acid alkyne (PAA)-CoA are added. The palmitoylation reaction is quenched at specific time points by N-ethylmaleimide (NEM), which both blocks the site of palmitoylation and the DHHC active-site cysteine. After washing, biotin-azide is clicked onto the palmitoylated substrate, which is subsequently eluted from the Ni-NTA plate and bound to anti-FLAG-coated plates. This allows the detection of the biotinylated substrate via fluorescence of Eu³⁺

+streptavidin and the determination of the steady-state rate of palmitoylation.

Examining DHHC18 and DHHC20 activity by OPPA. Using the VAMP7 and LAT constructs as palmitoylation targets and the DHHC18 and DHHC20 constructs as palmitoylating enzymes allowed us to validate the OPPA method and investigate these reactions *in vitro* (Fig. 2c). While autopalmitoylation of VAMP7 is minimal at 20 μ M PAA-CoA (Supplementary Figs. 6–8), the rate of palmitoylation is greatly enhanced by full-length DHHC18. The active-site mutant DHHC18-C222A prevents this palmitoylation. DHHC20 was barely capable of palmitoylating VAMP7, while its active-site mutant C156A is also inactive.

Truncating either the N- or C-terminal tails of DHHC18 results in a significant decrease in the palmitoylation rate of VAMP7. Whether this speaks for a role of these cytosolic tails in substrate recognition or engagement, in its enzymatic mechanism, or in simply stabilizing the enzyme will require further investigation. The short isoform DHHC18-2, lacking the N-terminal TMDs, is capable of palmitoylating VAMP7, albeit at a slightly decreased rate. Intriguingly, mutating the proposed palmitoylation anchor cysteine C138 to alanine prevents DHHC18-2's palmitoylation of VAMP7, while this mutation in full-length DHHC18-1 has no effect; one potential model to explain this is shown in Fig. 2b.

Finally, LAT was used as a second palmitoylation target. Full-length DHHC18 was capable of palmitoylating LAT, while DHHC20 failed to do so. This may speak to a specificity for LAT palmitoylation by DHHC18 and not DHHC20. As DHHC20 is located at the PM and turnover of LAT palmitoylation is not expected to be rapid, the specificity of Golgi-localized DHHC18 could perhaps reflect a biological reality; this should be confirmed in a cellular context, perhaps with PAT-specific knockouts and subsequent palmitome enrichment, as was recently performed for DHHC13^{45,48}.

VAMP7 palmitoylation is required for its localization. The proposed palmitoylation site in VAMP7, Cys183, was also mutated to alanine. This prevented its palmitoylation by both DHHC18 and DHHC20, suggesting that this is indeed the primary site of *in vitro* palmitoylation. To confirm this *in vivo*, CRISPR/Cas9-knockout Jurkat cell lines with lentivirally transduced stable re-expression of VAMP7-WT and -C183A constructs were engineered (Supplementary Fig. 10). Once generated, ABE was used to enrich all palmitoylated proteins in these cell lines. VAMP7 was found to be palmitoylated in the Jurkat E6.1 and VAMP7-WT re-expression cell lines, but not in the VAMP7-knockout or VAMP7-C183A re-expression cell lines, confirming that Cys183 is the site of VAMP7 palmitoylation in Jurkat T cells (Supplementary Fig. 11).

The VAMP7-KO Jurkat cell lines stably expressing VAMP7-WT and VAMP7-C183A were analyzed by confocal microscopy to observe localization of these two constructs. The re-expressed VAMP7-WT, which is capable of being palmitoylated, is largely found in the Golgi of the VAMP7-knockout/re-expression Jurkat cells, in agreement with earlier observations (Fig. 3a)⁴⁹. VAMP7-C183A, however, does not colocalize with the Golgi marker giantin, instead localizing to the cytosol, presumably within vesicles (Fig. 3). This supports the conclusion that palmitoylation of VAMP7 at Cys183 acts as a sorting signal for the Golgi^{50,51}. Mutating Cys183 prevents this localization, allowing a larger population of VAMP7 to localize to vesicles^{11,52}. Since it was shown previously that VAMP7 is localized to the immune synapse upon TCR activation^{11,52,53}, we tested if the palmitoylation of VAMP7 can affect its recruitment. We analyzed the

enrichment of VAMP7-WT and VAMP7-C183A in VAMP7-knockout/re-expressing Jurkat cells upon conjugate formation with Raji B cells. The Raji cells were left unpulsed or pulsed with the activating superantigen staphylococcus enterotoxin E (SEE) that binds and activates the TCR expressed by Jurkat cells. Quantification of the confocal microscopy images, as shown previously¹¹ showed that VAMP7-WT was enriched at the immune synapse in the presence of SEE (Fig. 3c, +SEE and average density map representation in a “mean cell” Fig. 3d and quantification in 3e). In contrast, the VAMP7-C183A mutant was fully compromised and did not get enriched at the immune synapse.

Altogether these results suggest that the palmitoylation of VAMP7 controls its localization in the Golgi at steady state and its recruitment to the immune synapse upon T-cell activation. Since VAMP7 has been shown to control membrane trafficking to and from the Golgi⁵⁴, mislocalization of the mutant form of VAMP7 may have downstream consequences for T-cell function such as polarized transport of proteins or cell migration. The fact that, as shown here, localization of this key v-SNARE protein is regulated upon TCR triggering reinforces the link that exists between TCR-induced signaling and intracellular trafficking⁵⁵.

Conclusions

In this study we capitalize on a proteomic screen for palmitoylated proteins that identifies clusters of G proteins, of vesicular transport proteins and of the DHHC palmitoyl transferases themselves. An OPPA was developed to probe the palmitoylation of individual sites in the palmitoyl acyltransferases as well as their target proteins. We show that VAMP7 can be palmitoylated at Cysteine-183 by DHHC18 *in vitro*, and that a palmitoylation-deficient mutant, VAMP7^{C183A}, when expressed in Jurkat T cells is localized away from the Golgi. Furthermore, this mutant is unable to be recruited to the immunological synapse formed between the T cell and Raji B cells upon superantigen stimulation. Thus, our screen provides an important basis for further investigations into the context between T-cell stimulation, DHHC enzyme activation, and vesicular transport.

Methods

Jurkat cell culture and stimulation. Jurkat T cells (clone E6-1) and Raji B (ATCC, CCL-86) cells were grown in RPMI 1640 SILAC medium with 10% FCS at 37 °C and 5% CO₂ (SILAC Quantification Kit, Pierce). Jurkat cells were stimulated using anti-CD3 IgM (C305) and anti-CD28 IgM hybridoma supernatants in RPMI without FCS at 37 °C; stimulation was quenched after 10 min by the addition of ice-cold PBS, centrifugation (300 \times g, 5 min, 4 °C), and subsequent shock-freezing of the cell pellets.

Generation of VAMP7-knockout in Jurkat cells. For the generation of sgRNAs the Atum online tool was used (<https://www.dna20.com/eCommerce/cas9/input>). The sgRNA oligos were then cloned into the pSpCas9(BB)-2A-GFP (PX458) vector (a kind gift from Feng Zhang [Addgene plasmid # 48138; <http://n2t.net/addgene:48138>; RRID:Addgene_48138]). Jurkat T cells (clone E6-1) were passaged to 0.125 Mio cells/ml the day before transfection. Five Mio cells were resuspended in 100 μ l OptiMem with 10 μ g pSpCas9(BB)-2A-GFP with the sgRNA CACCG-CACACCAAGCATGTTTGGCA and electroplated with a NEPA21 electroporator (Nepagene) with the following settings: 0.2 mm gap electroporation cuvettes, poring pulse: 175 V, length: 5 ms, interval: 50 ms, number: 2, D. rate: 10%; polarity: +. After 48 h single clones were sorted by FACS for EGFP into 96-well plates. After the cells had recovered and grown the knockout was validated by western blotting and sequencing.

Lentiviral transduction of Jurkat cells. Once the VAMP7-knockout cell line was validated, the re-expression of VAMP7 constructs was performed. Wildtype VAMP7 and mutant VAMP7-C183A, both featuring FLAG-tags, were cloned into the lentiviral vector LegoIG2 (a kind gift from Boris Fehse [Addgene plasmid # 27341; <http://n2t.net/addgene:27341>]; RRID:Addgene_27341)⁵⁶. HEK293 cells were transfected with the constructs FLAG-VAMP7-WT-LegoIG2 or FLAG-VAMP7-C183A-LegoIG2 plus the third-generation packaging plasmids pMDLg/pRRE with pRSV-Rev and pCMV-VSV-G using lipofectamine. Supernatants

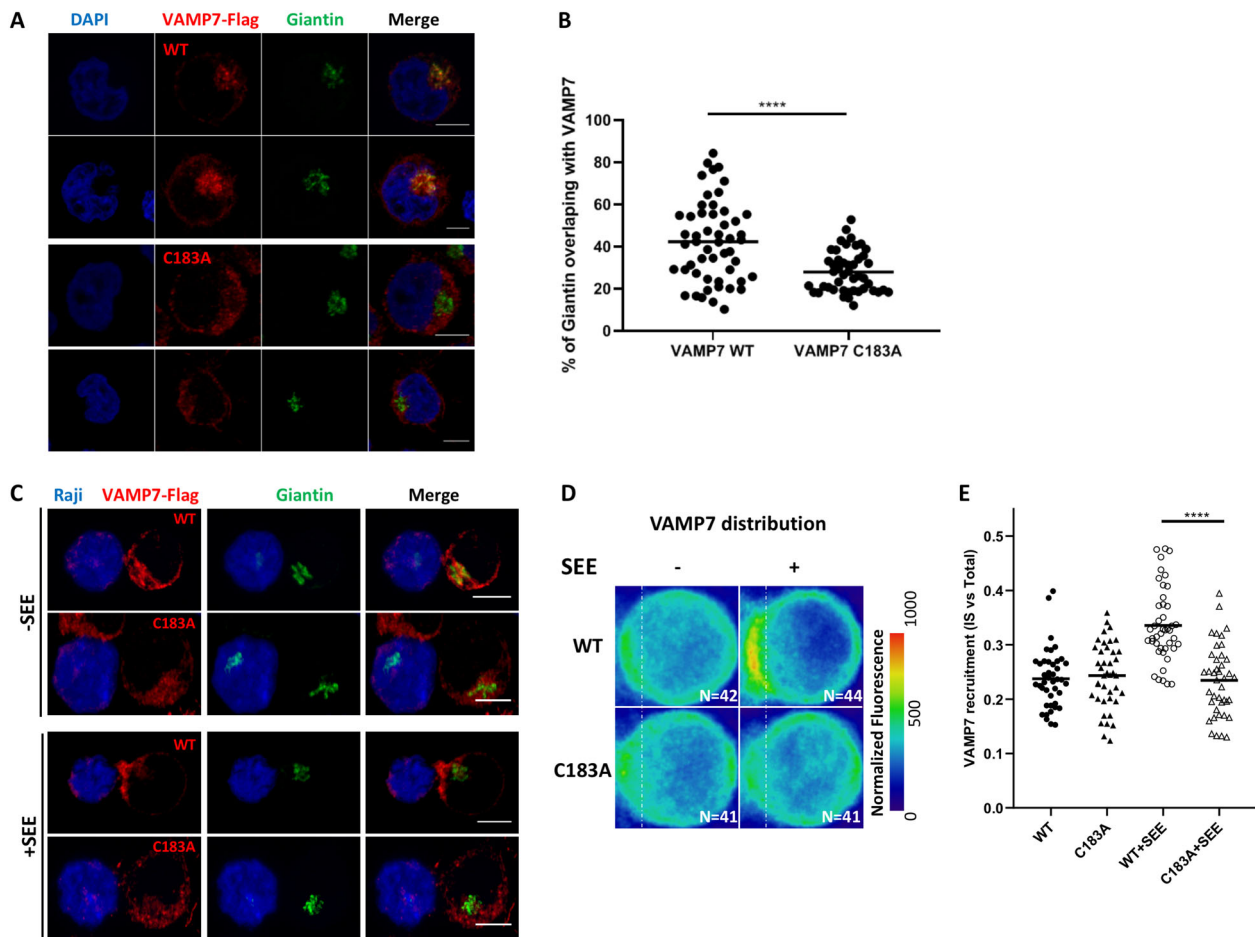


Fig. 3 The VAMP7-C183A mutant fails to properly localize to the Golgi. **a** Confocal images showing the relative localization of VAMP7 (red) labeled with anti-Flag Abs and Giantin (green) in VAMP7-KO Jurkat cells expressing the WT VAMP7-FLAG or the mutant VAMP7-C183A-FLAG proteins. Scale bar 5 μm . **b** Dot plots showing the quantification of the percentage of Giantin (Golgi marker) overlapping with the VAMP7-FLAG proteins (Manderson coefficient). Each dot = one cell; horizontal lines = median. **** $p < 0.0001$ (one-way ANOVA). **c** Representative confocal images of conjugates of Jurkat VAMP7-KO cells expressing the WT VAMP7-FLAG or the mutant VAMP7-C183A-FLAG proteins and SEE-pulsed Raji B cells (blue) labeled with anti-FLAG (VAMP7-FLAG, showed in red) or anti-Giantin (shown in green) antibodies, assessed at 15 min. Scale bar 5 μm . **d** Mapping and **e** quantification of the enrichment of VAMP7 at the immune synapse (depicted by the dotted white line) in Jurkat "mean cells" interacting for 15 min with Raji cells left unpulsed (-, inactivated state) or pulsed with SEE (+, immune synapse formation). N number of cells constituting the mean image. Horizontal lines represent median. Scale bar 5 μm . Each dot = one cell; horizontal lines = median. **** $p < 0.0001$ (t-test and one-way ANOVA). Data are from two independent experiments.

containing viruses were harvested after 48 h and concentrated by centrifugation at $10,000 \times g$ and 4°C for 4–6 h in glass tubes. VAMP7-knockout Jurkat cells were transduced with the viruses by spinoculation, as described previously⁵⁷. Cells were resuspended in lentiviral supernatant supplemented with Polybrene (6 $\mu\text{g}/\text{ml}$) and spun for 90 min at 37°C at a speed of $800 \times g$. After 72 h the cells were sorted by EGFP expression via FACS. One week later the cells were sorted again for EGFP expression and also for the expression of CD3 and CD28 surface markers.

Construct design and cloning. Primary sequences of VAMP7, LAT, DHHC18, and DHHC20 were obtained from UniProt. Full-length constructs of VAMP7 and LAT were engineered bearing His₆- and FLAG-tags, while DHHC18 and DHHC20 were designed with FLAG-tags alone, and ordered from Genart. Truncated constructs of DHHC18 were generated by amplifying FLAG-tagged inserts via PCR. Mutagenesis was performed using the QuikChange Site-Directed Mutagenesis system (Agilent). Constructs were then cloned into the pFastBac1 vector of the Bac-to-Bac system (Thermo Fisher).

Insect cell expression and purification. Sf9 insect cells were grown in Sf-900 II medium (Thermo Fisher) at 27°C . Baculoviruses were generated by transfecting insect cells with constructs in the pFastBac1 vector according to the Bac-to-Bac protocol. P4 viral stocks were then used to infect larger cultures, and expressed proteins were harvested 3–5 days following infection (~70–80% cell viability). Cell pellets were shock frozen and lysed in lysis buffer containing 50 mM NaH_2PO_4 (pH 7.2) (Roth), 300 mM NaCl (Roth), 0.2% Triton X-100 (Roth), 1

mM phenyl methanesulfonyl fluoride (PMSF) (Sigma), cComplete protease inhibitor cocktail (Roche), and DNase (New England BioLabs) and RNase (Pancreac AppliChem) on ice for 30 min. Lysates were cleared by centrifugation ($16,000 \times g$, 4°C , 10 min.) and supernatants were loaded onto anti-FLAG M2 affinity gel (Sigma) at 4°C . After washing, proteins were eluted using 0.1 M glycine at pH 3.5 and concentrated using Vivaspun spin filters (VWR) with appropriate MW cut-offs. After concentration, 0.08% n-dodecyl β -D-maltoside (DDM) (Sigma) and cComplete protease inhibitor cocktail was added and constructs were dialyzed overnight at 4°C into 50 mM NaH_2PO_4 (pH 6.5) and 10% glycerol (Roth). Protein concentration was determined by BCA assay (Pierce) and expression was confirmed by anti-FLAG western blot. Purified PATs were extremely sensitive to environmental conditions, precipitating at concentrations greater than ~5–10 μM and losing activity after freezing or 3–5 days storage at 4°C . For this reason, all purified PATs were used immediately for the OPPA assays following dialysis.

Western blotting. To confirm the stimulation via phosphotyrosine and phospho-ERK1/2, and to confirm expression/purification of constructs expressed in insect cells, lysates were run on SDS-PAGE gels and transferred to nitrocellulose membranes using standard methods. Antibodies used for detection: 4G10 Platinum anti-phosphotyrosine (Millipore), anti-pERK (E-4) (Santa Cruz), anti- β -actin (AC-15) (Sigma-Aldrich), anti-LAT (Upstate (Millipore)), and anti-FLAG-HRP (Sigma-Aldrich). The self-produced VAMP7 antibody was a kind gift of Dr. Andrew Peden (The University of Sheffield, UK).

Acyl-biotin exchange. The ABE protocol was followed as described previously^{31,58}. Briefly, stimulated Jurkat SILAC pellets were lysed in lysis buffer containing 50 mM Tris (pH 7.4) (Roth), 150 mM NaCl (Roth), 10 mM MgCl₂ (AppliChem), 10 mM KCl (Sigma–Aldrich), 500 μM EDTA (Roth), 100 μM Na₂VO₄ (Sigma–Aldrich), 20 mM NEM (Thermo), 1 mM PMSF, 1.7% Triton X-100, 1 mM tris(2-carboxyethyl)phosphine (TCEP) (Sigma–Aldrich), 100 μM methyl arachidonyl fluorophosphonate (MAFP) (Sigma–Aldrich), and cComplete protease inhibitor cocktail (PI-cocktail) on ice for 30 min. Lysates were cleared by centrifugation (16,100 × g, 4 °C, 10 min.). Chloroform-methanol (CM) precipitations were used between each chemical labeling step to ensure complete removal of unreacted reagents. The cleared lysates were subjected to a CM precipitation, then resuspended in buffer containing a 50 mM Tris (pH 7.4), 5 mM EDTA, 1% SDS (Roth), 125 mM NaCl, 1 mM PMSF, 0.2% Triton X-100, 20 mM NEM, and PI-cocktail and incubated overnight at 4 °C. NEM was then removed by three sequential CM precipitation steps, and enriched samples (e.g., heavy lysates) were resuspended in buffer containing 50 mM Tris (pH 7.4), 5 mM EDTA, 125 mM NaCl, 1% SDS, 574 mM hydroxylamine (HA) (Sigma–Aldrich), 820 μM EZ-Link HPDP-biotin (Thermo), 0.2% Triton X-100, 1 mM PMSF and PI-cocktail; control samples (e.g., light lysates) were resuspended in a similar buffer, omitting HA. After incubation for one hour at room temperature, a single CM precipitation removed HA, and samples were biotinylated in a buffer containing 50 mM Tris (pH 7.4), 5 mM EDTA, 125 mM NaCl, 164 μM EZ-Link HPDP-biotin, 0.2% Triton X-100, 1 mM PMSF, and PI-cocktail for 1 h at room temperature. Samples were then washed with three sequential CM precipitations and resuspended in buffer containing 50 mM Tris (pH 7.4), 5 mM EDTA, 125 mM NaCl, 0.1% SDS, 0.2% Triton X-100, 1 mM PMSF, and PI-cocktail. SILAC-labeled heavy and light samples were then mixed and allowed to bind to streptavidin-agarose beads (Novagen) for 90 min at room temperature. After four sequential washings, biotinylated peptides were eluted by cleaving the HPDP-biotin-cysteine disulfide linkage in a buffer containing 1% beta-mercaptoethanol (2-ME) (Roth) at 37 °C for 15 min. Eluates were precipitated via trichloroacetic acid (TCA) precipitation and resuspended in a smaller volume of SDS-PAGE sample buffer containing 0.2% Triton X-100, boiled for 5 min. at 95 °C, then run on a 4–12% Bis-Tris gel (NuPAGE Novex). After Coomassie staining, gels were used for in-gel tryptic digestion and subsequent LC-MS/MS. For the stimulated Jurkat cells, four individual ABE enrichments were performed ($n = 4$).

Quantitative LC-MS/MS and proteomic data analysis. Coomassie-stained gel lanes from the ABE enrichment were cut into 30 equal-sized bands and in-gel tryptic digest was performed as described previously³¹. Digested peptides were resuspended in 6 μl 0.1% (v/v) TFA and 5% (v/v) acetonitrile per band. Analysis of the peptides was performed via reversed-phase capillary liquid chromatography (Ultimate 3000 nanoLC system (Thermo Scientific)) coupled to an Orbitrap Elite mass spectrometer (Thermo Scientific). LC separations were performed on a capillary column (Acclaim PepMap100, C18, 3 μm, 100 Å, 75 μm i.d. × 25 cm, Thermo Scientific) at an eluent flow rate of 300 nL/min using a linear gradient of 3–25% B after 53 min with a further increase to 80% B after 80 min. Mobile phase A contained 0.1% formic acid in water, and mobile phase B contained 0.1% formic acid in acetonitrile. Mass spectra were acquired in a data-dependent mode with one MS survey scan with a resolution of 60,000 (Orbitrap Elite) and MS/MS scans of the 15 most intense precursor ions in the linear trap quadrupole were used. Raw data have been deposited at the ProteomeXchange Consortium via the PRIDE partner repository⁵⁹.

Identification and SILAC quantification were performed using MaxQuant software (version 1.4.1.1) with the Uniprot human protein database (2014 release). Proteins were filtered with the following criteria: (i) not identified only by site, reverse, or known contaminant (MaxQuant), (ii) at least one unique peptide, and (iii) at least two razor + unique peptides. The unstimulated Jurkat ABE enrichment we published earlier³¹ ($n = 6$) was reanalyzed using the following new procedure, allowing direct comparison to the stimulated Jurkat ABE dataset described here ($n = 4$). First, missing values were imputed with the median normalized heavy/light ratio of the specific LC-MS/MS run—in many cases this was very close to 1.0 (representing the background). H/L ratios were then transformed to log₂ values and the mean H/L ratio and one-sample *t*-test *p*-values were calculated. Volcano plots were generated plotting the log₂ fold-change to the $-\log_{10}(p)$ value, giving rise to a pool of high-confidence palmitoylated proteins. It should be noted that the median coefficient of variance (CV) from the stimulated dataset is higher (92%) than that of the unstimulated dataset (65%). To validate the enrichment of palmitoylated proteins under both conditions in an orthogonal way, enriched pools were analyzed based on three criteria, described previously³¹: (i) previous reports in other palmitoylation studies, (ii) predicted palmitoylation sites (CSSPalm 4.0), and (iii) predicted TMDs (TMDHMM 2.0)^{33,34}.

OPPA. Purified targets (VAMP7, LAT) were diluted to 1 μM in buffer containing 50 mM NaH₂PO₄ (pH 6.5), 500 mM NaCl, 1 mM TCEP and 0.08% DDM. For each time point (0, 5, 10, and 20 min), the diluted target was divided into 12 wells (50 μl each) of a 96-well Ni-NTA-coated plate (Pierce) and allowed to bind for 1 h. Palmitic acid alkyne (PAA)-CoA was generated by preparing 50 mM Tris (pH 8.1), 14 mM MgCl₂, 0.08% DDM, 0.1 mM EDTA, 1.6 mM ATP (Roth), 400 μM coenzyme A (Sigma), 40 μM PAA (Avanti), 0.05 UN/ml acyl-coenzyme A synthetase

(Sigma) and 1% BSA (Sigma) and incubating at 37 °C for 1 h. This was diluted two-fold (yielding [PAA-CoA] ~20 μM) with 0.3–2 μM purified DHHC PAT (or 1 μM BSA for negative control) with 150 mM NaH₂PO₄ (pH 6.5), 300 mM NaCl and 0.08% DDM. Ni-NTA plates were washed four times with PBS + 0.05% Tween-20 (Sigma–Aldrich) (PBST) using a plate washer (Tecan) and 100 μl of the enzyme mixture was added. Reactions were carried out at 37 °C with shaking for designated time points, and the reaction was quenched by washing with buffer containing 50 mM NaH₂PO₄ (pH 6.5), 300 mM NaCl, 40 mM NEM and 0.1% Triton X-100. After the complete time course, plates were washed four times with PBST and click chemistry was performed by the addition of 50 μl buffer containing 50 mM NaH₂PO₄ (pH 6.5), 300 mM NaCl, and 1% Triton X-100. Click chemistry reagents were added as described previously⁶⁰; briefly, to each 50 μl, the following reagents were added in this order, with vortexing between each step: 1 μl 1 mM biotin-azide (Thermo Fisher) in DMSO (Sigma), 1 μl 50 mM TCEP, 3 μl 16 mM Tris[(1-benzyl-1H-1,2,3-triazol-4-yl)methyl]amine (TBTA) (Sigma–Aldrich) prepared in 20% DMSO and 80% *t*-butanol (Sigma), and 1 μl 50 mM CuSO₄ (Sigma). Click chemistry was performed at 37 °C for 3 h with shaking. After washing the plate six times with PBST, palmitoylated targets were eluted with 100 μl buffer containing 50 mM NaH₂PO₄ (pH 6.5), 300 mM NaCl, 1% Triton X-100, 1 mM EDTA and 200 mM imidazole (Roth) for 30 min at 37 °C. Eluates were transferred to high-binding plates (Greiner) coated for 3 h at room temperature with monoclonal anti-FLAG (Sigma–Aldrich) and blocked for 2 h at room temperature with 3% BSA and allowed to bind overnight at 4 °C with shaking. Plates were then washed six times with PBST and buffer containing PBS and 0.2 μg/ml Eu³⁺-streptavidin (PerkinElmer) and incubated at room temperature for 1 h. After washing eight times with PBST, fluorescence was measured in 120 μl enhancer solution (15 μM beta-naphthoyltrifluoroacetone (Sigma), 50 μM tri-*n*-cotylphosphine oxide (Sigma), 6.8 mM potassium hydrogen phthalate (Roth), 100 mM acetic acid (Roth) and 0.1% Triton X-100) using a plate reader (Victor³V, PerkinElmer) with excitation and emission wavelengths of 340 nm and 614 nm, respectively. All measured fluorescence values were normalized to both the $t = 0$ fluorescence value and the μg of protein (DHHC PAT or BSA) used in the reaction, and steady-state rates were calculated over the 20-min reaction time.

Immunofluorescence. Coverslips and dishes preparation: 12mmø coverslips (VWR, 631-0666) were precoated with 0.02% of poly-L-Lysine for 20 min at room temperature and were washed 3 times in water before being dried and kept for maximum 2 days. 100,000 cells were incubated on coverslips for 30 min in PBS.

Preparation of Jurkat T cells and Raji B cells conjugates: Raji B cells were washed, resuspended at a concentration of 1×10^6 cells/mL in RPMI without FCS and labeled with CellTracker™ Blue CMAC dye (10 μM, Thermo Fisher, C2110) for 20 min at 37 °C. Labeling was stopped with RPMI 10% FCS and cells were washed once and resuspended at 1×10^6 cells/mL. Cells were pulsed with SEE (100 ng/mL) or left untreated for 30 min at 37 °C before being washed once and resuspended at a concentration of 1×10^6 cells/mL. 100,000 Raji cells were incubated on coverslips for 30 min, washed once with warm PBS and 150,000 Jurkat cells resuspended in RPMI 10% FCS were added for 15 min. Coverslips were washed once with cold PBS before fixation.

Fixation: Cells were fixed with 4% paraformaldehyde (Life Technologies, FB002) for 15 min at room temperature, washed once in PBS and excess of paraformaldehyde was quenched for 10 min with PBS 10 mM glycine (Thermo Fisher Scientific, G8898). Coverslips were kept at 4 °C in PBS until permeabilization and staining.

Staining: Cells were permeabilized for 30 min at room temperature with PBS + 0.2% Bovine Serum Albumin (BSA, Euromedex, 04-100-812) and 0.05% Saponin (Sigma–Aldrich, S4521). Cells were then incubated for 1 h at room temperature with primary antibody, then washed three times with PBS 0.2% BSA 0.05% Saponin and incubated protected from light for 20 min in the same buffer with spun secondary antibodies. After washing once with PBS BSA Saponin, and once with PBS, coverslips were soaked three times in PBS, three times in water, and mounted on slides.

Mounting: For regular confocal microscopy, coverslips were mounted with 4–6 μl Fluoromount G (SouthernBiotech, 0100-01) on slides (KNITTEL Starfrost) and dried overnight protected from light before microscope acquisition.

Microscope: Images were acquired with a Leica Dmi8 inverted microscope equipped with an SP8 confocal unit using either a ×40(1.35NA) or ×63(1.4NA) objective. Single plane images or Z-stack of images were acquired (pixel size around 60 nm).

Analysis of VAMP7 colocalization with Giantin: Z-stack (0.5 μm) images of similarly dimensioned Jurkat cells were chosen. In this z-stack, an ROI surrounding the Golgi was defined based on Giantin staining. Within each ROI, masks based on both Giantin and VAMP7 stainings were created by thresholding. Automatic colocalization assays were performed with Mander's overlap coefficient, using the JACoP plugin for ImageJ64.

Antibodies: Anti-Flag (1/100) was from Sigma–Aldrich (F3165). Anti-Giantin (1/100) was produced by the recombinant antibody platform of the Institut Curie, Paris, France. Anti-rabbit Ig Alexa Fluor 488 (1/200) and anti-mouse Ig Alexa Fluor 568 (1/200) antibodies were from Thermo Fisher Scientific (A11034 and A11004 respectively).

Recruitment at the immune synapse and “Mean Cell” creation: Single images corresponding to the middle planes of conjugates were extracted from Z-stack. T cells were cropped and oriented in the same way regarding their synapse (script#1). Obtained T-cell images were grouped by condition (WT/C183A ± SEE) and fluorescence intensities were normalized by the mean fluorescence intensity (MFI). Images were then resized to the smallest image size in order to create a normalized stack of images for each group (script#2). All groups were normalized (size and intensity) before being compared. Stacks of aligned cells were finally projected (averaging method) giving single plane “mean cells” (script#3). Stacks were resized to obtain a 1-pixel height stack by averaging the fluorescence intensity of the total height of each image. Projections of the 1-pixel resized stacks were obtained based on average and standard deviation methods and pixel intensities profiles were performed along projections width (script#4). In order to get a cell-by-cell quantification, we also computed an enrichment ratio at the synapse. This enrichment was defined as the ratio between the total cell fluorescence and the fluorescence in the synaptic region (rectangle at the synapse representing 20% of the total cell). (script#3).

Statistics and reproducibility. The proteomic experiments of ABE-labeled experiments were performed with four biological replicates. Heavy/light SILAC ratios were calculated using MaxQuant software and mean values and one-sample *t*-test *p*-values were calculated for the volcano plot analysis. OPPA experiments were performed with $n \geq 12$ technical replicates on each plate for each time point, and geometric means and standard errors of the mean were calculated for each condition.

Reporting summary. Further information on research design is available in the Nature Research Reporting Summary linked to this article.

Data availability

The mass spectrometry proteomics data have been deposited to the ProteomeXchange Consortium via the PRIDE partner repository⁵⁹ with the dataset identifiers PXD018710 and PXD018703. Supplementary Data 1 contains proteins enriched via ABE in unstimulated and/or anti-CD3/anti-CD28 costimulated (10-min) Jurkat T cells. Source data are available as Supplementary Data 2 and 3. All other data are available from the corresponding author on reasonable request.

Received: 6 November 2019; Accepted: 19 May 2020;

Published online: 10 July 2020

References

- Ladygina, N., Martin, B. R. & Altman, A. Dynamic palmitoylation and the role of DHHC proteins in T cell activation and anergy. *Adv. Immunol.* **109**, 1–44 (2011).
- Resh, M. D. Fatty acylation of proteins: the long and the short of it. *Prog. Lipid Res.* **63**, 120–131 (2016).
- Lin, D. T. S. & Conibear, E. ABHD17 proteins are novel protein depalmitoylases that regulate N-Ras palmitate turnover and subcellular localization. *elife* **4**, e11306 (2015).
- Fukata, Y. & Fukata, M. Protein palmitoylation in neuronal development and synaptic plasticity. *Nat. Rev. Neurosci.* **11**, 161–175 (2010).
- Fukata, Y. et al. Local palmitoylation cycles define activity-regulated postsynaptic subdomains. *J. Cell Biol.* **202**, 145–161 (2013).
- El-Husseini, A. E. D. et al. Synaptic strength regulated by palmitate cycling on PSD-95. *Cell* **108**, 849–863 (2002).
- Baker, T. L., Zheng, H., Walker, J., Coloff, J. L. & Buss, J. E. Distinct rates of palmitate turnover on membrane-bound cellular and oncogenic H-Ras. *J. Biol. Chem.* **278**, 19292–19300 (2003).
- Smotrys, J. E. & Linder, M. E. Palmitoylation of intracellular signaling proteins: regulation and function. *Annu. Rev. Biochem.* **73**, 559–587 (2004).
- Akimzhanov, A. M. & Boehning, D. Rapid and transient palmitoylation of the tyrosine kinase Lck mediates Fas signaling. *Proc. Natl Acad. Sci. USA* **2015**, 201509929 (2015).
- Hundt, M. et al. Impaired activation and localization of LAT in anergic T cells as a consequence of a selective palmitoylation defect. *Immunity* **24**, 513–522 (2006).
- Larghi, P. et al. VAMP7 controls T cell activation by regulating the recruitment and phosphorylation of vesicular Lat at TCR-activation sites. *Nat. Immunol.* **14**, 723–731 (2013).
- Prescott, G. R., Gorleku, O. A., Greaves, J. & Chamberlain, L. H. Palmitoylation of the synaptic vesicle fusion machinery. *J. Neurochem.* **110**, 1135–1149 (2009).
- Lobo, S., Greentree, W. K., Linder, M. E. & Deschenes, R. J. Identification of a Ras palmitoyltransferase in *Saccharomyces cerevisiae*. *J. Biol. Chem.* **277**, 41268–41273 (2002).
- Roth, A. F., Feng, Y., Chen, L. & Davis, N. G. The yeast DHHC cysteine-rich domain protein Akrlp is a palmitoyl transferase. *J. Cell Biol.* **159**, 23–28 (2002).
- Jennings, B. C. & Linder, M. E. DHHC protein S-acyltransferases use similar ping-pong kinetic mechanisms but display different Acyl-CoA specificities. *J. Biol. Chem.* **287**, 7236–7245 (2012).
- Mitchell, D. A. et al. Mutations in the X-linked intellectual disability gene, *zDHHC9*, alter autopalmitylation activity by distinct mechanisms. *J. Biol. Chem.* **289**, 18582–18592 (2014).
- Fukata, M., Fukata, Y., Adesnik, H., Nicoll, R. A. & Bredt, D. S. Identification of PSD-95 palmitoylating enzymes. *Neuron* **44**, 987–996 (2004).
- Rana, M. S. et al. Fatty acyl recognition and transfer by an integral membrane S-acyltransferase. *Science* **359**, eao6326 (2018).
- Korycka, J. et al. Human DHHC proteins: a spotlight on the hidden player of palmitoylation. *Eur. J. Cell Biol.* **91**, 107–117 (2012).
- Kriegenburg, F., Bas, L., Gao, J. & Ungermann, C. The multi-functional SNARE protein Ykt6 in autophagosomal fusion processes. *Cell Cycle* **0**, 1–13 (2019).
- Won, S. J. & Martin, B. R. Temporal profiling establishes a dynamic S-palmitoylation cycle. *ACS Chem. Biol.* **13**, 1560–1568 (2018).
- Thinon, E., Fernandez, J. P., Molina, H. & Hang, H. C. Selective enrichment and direct analysis of protein S-palmitoylation sites. *J. Proteome Res.* **17**, 1907–1922 (2018).
- Hernandez, J. L. et al. Correlated S-palmitoylation profiling of Snail-induced epithelial to mesenchymal transition Jeannie. *Mol. Biosyst.* **12**, 1799–1808 (2016).
- Serwa, R. A. et al. Systems analysis of protein fatty acylation in Herpes simplex virus-infected cells using chemical proteomics. *Chem. Biol.* **22**, 1008–1017 (2015).
- Peng, T., Thinon, E. & Hang, H. C. Proteomic analysis of fatty-acylated proteins. *Curr. Opin. Chem. Biol.* **30**, 77–86 (2016).
- Xiaochao, W. et al. Insulin-regulated protein palmitoylation impacts endothelial cell function. *Arterioscler. Thromb. Vasc. Biol.* **34**, 346–354 (2014).
- Ivaldi, C. et al. Proteomic analysis of S-Acylated proteins in human B cells reveals palmitoylation of the immune regulators CD20 and CD23. *PLoS ONE* **7**, 1–9 (2012).
- Dowal, L., Yang, W., Freeman, M. R., Steen, H. & Flaumenhaft, R. Proteomic analysis of palmitoylated platelet proteins. *Blood* **118**, 2–4 (2011).
- Yang, W. et al. Proteome scale characterization of human S-acylated proteins in lipid raft-enriched and non-raft membranes. *Mol. Cell. Proteom.* **9**, 54–70 (2010).
- Martin, B. R. & Cravatt, B. F. Large-scale profiling of protein palmitoylation in mammalian cells. *Nat. Methods* **6**, 135–138 (2009).
- Morrison, E. et al. Quantitative analysis of the human T cell palmitome. *Sci. Rep.* **5**, 11598 (2015).
- Blaskovic, S., Blanc, M. & Goot, F. G. VanDer. What does S-palmitoylation do to membrane proteins? *FEBS J.* **280**, 2766–2774 (2013).
- Ren, J. et al. CSS-Palm 2.0: an updated software for palmitoylation sites prediction. *Protein Eng. Des. Sel.* **21**, 639–644 (2008).
- Krogh, A., Larsson, B., von Heijne, G. & Sonnhammer, E. L. Predicting transmembrane protein topology with a hidden markov model: application to complete genomes. *J. Mol. Biol.* **305**, 567–580 (2001).
- Colquhoun, D. R. et al. Bioorthogonal mimetics of palmitoyl-CoA and myristoyl-CoA and their subsequent isolation by click chemistry and characterization by mass spectrometry reveal novel acylated host-proteins modified by HIV-1 infection. *Proteomics* **15**, 2066–2077 (2015).
- Fang, C. et al. Identification of palmitoylated transitional endoplasmic reticulum ATPase by proteomic technique and pan antipalmitoylation antibody. *J. Proteome Res.* **15**, 956–962 (2016).
- Pinner, A. L., Tucholski, J., Haroutunian, V., McCullumsmith, R. E. & Meador-Woodruff, J. H. Decreased protein S-palmitoylation in dorsolateral prefrontal cortex in schizophrenia. *Schizophr. Res.* **177**, 78–87 (2016).
- Peng, T. & Hang, H. C. Bifunctional fatty acid chemical reporter for analyzing S-palmitoylated membrane protein-protein interactions in mammalian cells. *J. Am. Chem. Soc.* **137**, 556–559 (2015).
- Xiaochao, W., Song, H. & Semenkovich, C. F. Insulin-regulated protein palmitoylation impacts endothelial cell function. *Arterioscler. Thromb. Vasc. Biol.* **34**, 346–354 (2014).
- Wilson, J. P., Raghavan, A. S., Yang, Y.-Y., Charron, G. & Hang, H. C. Proteomic analysis of fatty-acylated proteins in mammalian cells with chemical reporters reveals S-acylation of histone H3 variants. *Mol. Cell. Proteom.* **10**, M110.001198 (2011).
- Forrester, M. T. et al. Site-specific analysis of protein S-acylation by resin-assisted capture (Acyl-RAC). *J. Lipid Res.* **52**, 393–398 (2011).

42. Marin, E. P., Derakhshan, B., Lam, T. T., Davalos, A. & Sessa, W. C. Endothelial cell palmitoylproteomics identifies novel lipid modified targets and potential substrates for protein acyl transferases. *Circ. Res.* **110**, 1336–1344 (2012).
43. Yang, W., Vizio, D. D. I., Kirchner, M., Steen, H. & Freeman, M. R. Proteome scale characterization of human S-acylated proteins in lipid raft-enriched and non-raft membranes. *Mol. Cell. Proteom.* **9**, 54–70 (2010).
44. Tsutsumi, R., Fukata, Y. & Fukata, M. Discovery of protein-palmitoylating enzymes. *Pflug. Arch. Eur. J. Physiol.* **456**, 1199–1206 (2008).
45. Ohno, Y. et al. Intracellular localization and tissue-specific distribution of human and yeast DHHC cysteine-rich domain-containing proteins. *Biochim. Biophys. Acta Mol. Cell Biol. Lipids* **1761**, 474–483 (2006).
46. Mitchell, D. A., Mitchell, G., Ling, Y., Budde, C. & Deschenes, R. J. Mutational analysis of *Saccharomyces cerevisiae* Erf2 reveals a two-step reaction mechanism for protein palmitoylation by DHHC enzymes. *J. Biol. Chem.* **285**, 38104–38114 (2010).
47. Hernandez, J. L. et al. APT2 inhibition restores scribble localization and S-Palmitoylation in snail-transformed cells. *Cell Chem. Biol.* **24**, 87–97 (2017).
48. Shen, L. et al. Role of S-palmitoylation by ZDHHC13 in mitochondrial function and metabolism in liver. *Sci. Rep.* **7**, 2182 (2017).
49. Zucchetti, A. E. et al. Tethering of vesicles to the Golgi by GMAP210 controls LAT delivery to the immune synapse. *Nat. Commun.* **10**, 2864 (2019).
50. Ernst, A. M. et al. S-palmitoylation sorts membrane cargo for anterograde transport in the Golgi article S-palmitoylation sorts membrane cargo for anterograde transport in the Golgi. *Dev. Cell* **47**, 479–493 (2018).
51. Rocks, O., Peyker, A. & Bastiaens, P. I. Spatio-temporal segregation of Ras signals: one ship, three anchors, many harbors. *Curr. Opin. Cell Biol.* **18**, 351–357 (2006).
52. Balagopalan, L. et al. Plasma membrane LAT activation precedes vesicular recruitment defining two phases of early T-cell activation. *Nat. Commun.* **9**, 2013 (2018).
53. Soares, H. et al. Regulated vesicle fusion generates signaling nanoterritories that control T cell activation at the immunological synapse. *J. Exp. Med.* **210**, 2415–2433 (2013).
54. Chaineau, M., Danglot, L. & Galli, T. Multiple roles of the vesicular-SNARE TI-VAMP in post-Golgi and endosomal trafficking. *FEBS Lett.* **583**, 3817–3826 (2009).
55. Saveanu, L., Zucchetti, A. E., Evnouchidou, I., Ardouin, L. & Hivroz, C. Is there a place and role for endocytic TCR signaling? *Immunol. Rev.* **291**, 57–74 (2019).
56. Weber, K., Bartsch, U., Stocking, C. & Fehse, B. A multicolor panel of novel lentiviral “Gene Ontology” (LeGO) vectors for functional gene analysis. *Mol. Ther.* **16**, 698–706 (2008).
57. Álvaro-Benito, M., Morrison, E., Abualrous, E. T., Kuroпка, B. & Freund, C. Quantification of HLA-DM-dependent major histocompatibility complex of class II immunopeptidomes by the peptide landscape antigenic epitope alignment utility. *Front. Immunol.* **9**, 872 (2018).
58. Drisdell, R. C. & Green, W. N. Labeling and quantifying sites of protein palmitoylation. *Biotechniques* **36**, 276–285 (2004).
59. Perez-Riverol, Y. et al. The PRIDE database and related tools and resources in 2019: improving support for quantification data. *Nucleic Acids Res.* **47**, D442–D450 (2019).
60. Martin, B. R. Nonradioactive analysis of dynamic protein palmitoylation. *Curr. Protoc. Protein Sci.* **73**, 1–9 (2013).

Acknowledgements

We would like to give special thanks to Frank Kuppler, Ellie Fox, Michael Schümann, Benno Kuroпка and Heike Stephanowitz for technical support, also special thanks to Andrew Peden (The University of Sheffield, UK) for gifting us the anti-VAMP7 antibodies. C.F. and B.B. are supported by the DFG (TRR186, Project A05). C.H. is supported by funds from Institut Curie, Institut National de la Santé et de la Recherche Médicale (INSERM) and ANR (ANR-10-IDEX-0001-02 PSL*, and ANR-11-LABX-0043).

Author contributions

C.F., B.B., C.H., and E.M. conceived the research. E.M., T.W., A.E.Z., M.A.B., and A.Z. performed the experiments and analyzed the data with input and support from E.K., S.F., B.B., C.H., and C.F. E.M. wrote the manuscript with critical input from C.F. and corrections from all other authors.

Competing interests

The authors declare no competing interests.

Additional information

Supplementary information is available for this paper at <https://doi.org/10.1038/s42003-020-1063-5>.

Correspondence and requests for materials should be addressed to C.F.

Reprints and permission information is available at <http://www.nature.com/reprints>

Publisher's note Springer Nature remains neutral with regard to jurisdictional claims in published maps and institutional affiliations.



Open Access This article is licensed under a Creative Commons Attribution 4.0 International License, which permits use, sharing, adaptation, distribution and reproduction in any medium or format, as long as you give appropriate credit to the original author(s) and the source, provide a link to the Creative Commons license, and indicate if changes were made. The images or other third party material in this article are included in the article's Creative Commons license, unless indicated otherwise in a credit line to the material. If material is not included in the article's Creative Commons license and your intended use is not permitted by statutory regulation or exceeds the permitted use, you will need to obtain permission directly from the copyright holder. To view a copy of this license, visit <http://creativecommons.org/licenses/by/4.0/>.

© The Author(s) 2020